Computer Vision and Image Understanding 125 (2014) 237–250

Contents lists available at ScienceDirect

Computer Vision and Image Understanding

journal homepage: www.elsevier.com/locate/cviu

Fast and globally convex multiphase active contours for brain MRI segmentation ☆

Juan C. Moreno [a,*], V.B. Surya Prasath [b], Hugo Proença [a], K. Palaniappan [b]

[a] IT: Instituto de Telecomunicações, University of Beira Interior, 6201-001 Covilha, Portugal
[b] Department of Computer Science, University of Missouri-Columbia, MO 65211, USA

ARTICLE INFO

Article history:
Received 28 August 2013
Accepted 24 April 2014
Available online 9 May 2014

Keywords:
Image segmentation
Active contours
Multiphase
Globally convex
Dual formulation
Brain MRI

ABSTRACT

Multiphase active contour based models are useful in identifying multiple regions with spatial consistency but varying characteristics such as the mean intensities of regions. Segmenting brain magnetic resonance images (MRIs) using a multiphase approach is useful to differentiate white and gray matter tissue for anatomical, functional and disease studies. Multiphase active contour methods are superior to other approaches due to their topological flexibility, accurate boundaries, robustness to image variations and adaptive energy functionals. Globally convex methods are furthermore initialization independent. We extend the relaxed globally convex Chan and Vese two-phase piecewise constant energy minimization formulation of Chan et al. (2006) [1] to the multiphase domain and prove the existence of a global minimizer in a specific space which is one of the novel contributions of the paper. An efficient dual minimization implementation of our binary partitioning function model accurately describes disjoint regions using stable segmentations by avoiding local minima solutions. Experimental results indicate that the proposed approach provides consistently better accuracy than other related multiphase active contour algorithms using four different error metrics (Dice, Rand Index, Global Consistency Error and Variation of Information) even under severe noise, intensity inhomogeneities, and partial volume effects in MRI imagery.

1. Introduction

The aim of image segmentation is to obtain meaningful partitions of an input image into a finite number of disjoint homogeneous objects. Active contour models are popular in the regard. Chan and Vese [2] proposed an active contour without edges scheme based on the classical work of Mumford and Shah [3] variational energy minimization model. Since biomedical images typically have multiple regions of interest with different characteristics, deriving a multiphase active contour scheme for efficient segmentation is an important area of research in image processing [4–6].

Measuring brain activity and structure using neuroimaging, combined with behavioral and genetic data to characterize human brain connectivity is one of the major goals of The Human Connectome Project (HCP) [7]. Systematic processing and analysis of the MRI (magnetic resonance image) data collected by the HCP for 1200 subjects will be an extremely challenging task. Automated segmentation of multimodal imagery such as T1-weighted, T2-weighted anatomical scans, diffusion imaging, resting state and task-evoked functional MRI will enable quantitative characterization of similarities and differences in structural connectivity and brain activity differences between individuals. Cognitive processes such as memory, language, emotion, decision-making, and social cognition are all being studied as part of the HCP. One of the basic quantitative image analysis tasks that is expected to be necessary in the neuro-informatics data processing workflow is brain region segmentation. The multi-region brain MRI segmentation algorithm developed in this paper will facilitate the large scale efforts underway in functional connectomics and can be adapted for building an activity map of the brain.

In MR images, segmentation schemes based on active contours have used the traditional level set method [8]. Active contours can also be improved using region information [9,10], salient features [11], mathematical morphology [12], etc. Traditionally these schemes use a gradient descent formulation to implement the non-convex energy minimization which often converges to undesirable local minima resulting in erroneous segmentations.

☆ This paper has been recommended for acceptance by Isabelle Bloch.

* Corresponding author.
E-mail addresses: jcmb@ubi.pt (J.C. Moreno), prasaths@missouri.edu (V.B. Surya Prasath), hugomcp@ubi.pt (H. Proença), palaniappank@missouri.edu (K. Palaniappan).

http://dx.doi.org/10.1016/j.cviu.2014.04.010
1077-3142/

Moreover, traditional level set based implementations are susceptible to slower convergence due to the well-known re-initialization requirement and discretization errors. Among other techniques for MRI segmentation, we mention fuzzy C-means based models [13–16], fuzzy connectedness [17], automatic labeling [18], adaptive expectation–maximization (EM) [19], Bayesian EM [20], hidden Markov model EM [21], kernel clustering [22], optimum-path clustering [23], anisotropic diffusion combined with classical snakes model [24], discriminant analysis [25], and neural networks [26]. We also refer to [27–29] for reviews about segmentation for medical images in general. The area of MRI image segmentation has seen tremendous research activity and a more detailed review in this particular field can be found in [30].

Recently quite a lot of interest is being shown in techniques that can obtain a general convex formulation for active contours schemes based on energy minimization which can alleviate the problem of local minima and at the same time reduce computational complexity [31–37]. In Chan et al. [1] a convex approach to the two phase segmentation is proposed when the piecewise constant values labeling disjoint regions are known. The method relies in replacing the Heaviside functions of level sets (or characteristic functions) by convex and differentiable functions varying in the interval $[0,1]$ which remarkably still yields a solution that is obtained by a simple thresholding procedure. This allows the non-convex Chan–Vese problem [2] to be solved using standard convex optimization methods. There have been efforts to extend the approach of [1] to the more challenging multi-phase problem [5]. Zach et al. [38] and Lellman et al. [39] proposed convex minimization schemes for the multi-phase segmentation without guaranteed global optimum of the original problem. Other approaches due to [40,41] not only use a convex formulation but also a dual formulation of the total variation in order to enforce a convex constraint on the dual variable providing accurate and better numerical solutions, but do not aim at computing a global minimizer of the problem.

In this paper, we consider a globally convex version of the four phase piecewise constant energy functional motivated from the seminal work of Chan et al. [1] and based on Bresson et al. [42] which considered the two phase segmentation model. By deriving an approximate novel convex functional we change the original formulation into a binary segmentation problem and utilize a Chambolle's dual minimization [43] to solve the relaxed formulation [44]. The proposed global methodology avoids the level set re-initialization constraint and other ad hoc techniques [45] used for fixing level set active contour movements throughout the iterations. The proposed approach is used to obtain white matter and gray matter partitions on brain MRI images as can be seen for example in Fig. 1. Fig. 1a is a coronal slice from a normal brain MRI and the binary segmentations capture gray matter/white matter (Fig. 1b white and black regions respectively), and tissue/background (Fig. 1c white and black regions respectively). Fig. 1d show the final segmentation result as contours superimposed on the input image and the color coded regions in Fig. 1e shows that our scheme captures the intermediate regions as well.

Our scheme does not involve level sets or re-initialization and instead relies on the relaxed globally convex formulation of the Vese and Chan multiphase active contours [5]. Comparison results on different MRI data sets (real and synthetic) with varying noise and inhomogeneities show that we can obtain better results than traditional level set multiphase schemes [5,46,47] and the primal–dual approach of [48]. Moreover, compared to these traditional level set based implementations we achieve faster convergence due to the use of efficient alternating dual minimization [49]. The proposed approach is general in the sense that we can add domain specific knowledge to improve such active contour schemes further for various tasks [50–55]. The main contribution of our work is twofold: (1) a fast four phase active contour model using a relaxed globally convex minimization approximation; (2) an efficient dual minimization based numerical implementation for performing segmentation on MRI images.

The rest of the paper is organized as follows. Section 2 introduces the multiphase variational active contour scheme and provides a globally convex formulation. Section 3 illustrates the segmentation results on various Brain MRI images including comparison of different schemes. Finally, Section 4 concludes the paper with discussion.

2. Multiphase active contours model

2.1. Finding the global minimum

We first briefly review the classical level set formulation of Chan and Vese [2] which is based on the Mumford and Shah functional [3] with particular emphasis on the piecewise constant model. The Mumford–Shah segmentation energy minimization is given by

$$\min_{c_0,c_1\in\mathbb{R},\Sigma\subset\Omega} MS(\Sigma,c_0,c_1) := Per(\Sigma) + \lambda_0 \int_{\Sigma} (I-c_0)^2 d\mathbf{x} + \lambda_1 \int_{\Omega\setminus\Sigma} (I-c_1)^2 d\mathbf{x} \tag{1}$$

where $I:\Omega\subset\mathbb{R}^2\to\mathbb{R}$ is the input image, $Per(\cdot)$ denotes the perimeter and $\partial\Sigma$ separates the regions Σ and $\Omega\setminus\Sigma$ where the two values c_0, c_1 are taken. This functional is non-convex even if we fix the constants c_0, c_1 and thus a difficult optimization problem. Chan and Vese proposed to use the level set-based algorithm for solving the functional (1) by representing the boundary $\partial\Sigma$ with the zero level set of an implicit function which models the image. Let $\phi:\Omega\subset\mathbb{R}^2\to\mathbb{R}$ be the level set which defines two regions which are 'inside' $\{\mathbf{x}\in\Omega:\phi(\mathbf{x})<0\}$ and 'outside' $\{\mathbf{x}\in\Omega:\phi(\mathbf{x})>0\}$ based on the zero level set $\phi=0$. Let H is the Heaviside function,

$$H(z) = \begin{cases} 1 & \text{if } z\geqslant 0, \\ 0 & \text{if } z<0. \end{cases} \tag{2}$$

(a) (b) (c) (d) (e)

Fig. 1. Our fast and automatic four phase image segmentation scheme provides a better segmentation for brain MRI images, it differentiates the gray matter from the surrounding white region clearly. (a) Input image, coronal slice from a normal brain MR imagery. (b) and (c) Show final binary segmentations obtained by thresholding the relaxed functions u_1, u_2 at 0.5, (d) Final segmentation result showing the contours superimposed on the input image. (e) Color coded visualization of the obtained segmentation result. (For interpretation of the references to color in this figure legend, the reader is referred to the web version of this article.)

Then the Chan and Vese model is given by the following minimization problem,

$$\min_{(\mathbf{c},\phi)} E(\mathbf{c},\phi) = \int_\Omega \delta(\phi)|\nabla\phi|d\mathbf{x} + \lambda_0\int_\Omega (I-c_0)^2 H(\phi)d\mathbf{x} + \lambda_1\int_\Omega (I-c_1)^2(1-H(\phi))d\mathbf{x}, \quad (3)$$

where δ is the Dirac delta function, $\mathbf{c} = (c_0, c_1)$ are the mean intensity values inside and outside regions respectively. The Euler–Lagrange equation with gradient descent formulation results in a nonlinear partial differential equation (PDE),

$$\frac{\partial\phi}{\partial t} = \delta(\phi)\left(div\left(\frac{\nabla\phi}{|\nabla\phi|}\right) - \lambda_0(I-c_0)^2 + \lambda_1(I-c_1)^2\right), \quad (4)$$

along with

$$c_0 = \frac{\int_\Omega IH(\phi)d\mathbf{x}}{\int_\Omega H(\phi)d\mathbf{x}}, \quad c_1 = \frac{\int_\Omega I(1-H(\phi))d\mathbf{x}}{\int_\Omega (1-H(\phi))d\mathbf{x}}. \quad (5)$$

Chan et al. [1] in their work on finding global minimizers for such segmentation models observed that the following PDE,

$$\frac{\partial\phi}{\partial t} = \left(div\left(\frac{\nabla\phi}{|\nabla\phi|}\right) - \lambda_0(I-c_0) + \lambda_1(I-c_1)\right), \quad (6)$$

and the PDE in Eq. (4) has the same steady states and the later PDE (6) can be derived from the following functional,

$$\min_{(\mathbf{c},\phi)} \mathcal{E}(\mathbf{c},\phi) = \int_\Omega |\nabla\phi|d\mathbf{x} + \int_\Omega [\lambda_0(I-c_0)^2 - \lambda_1(I-c_1)^2]\phi d\mathbf{x}. \quad (7)$$

The following theorem which is proven in [1] paves the way for obtaining globally convex version of the two phase Mumford and Shah functional.

Theorem 1 Theorem 2 in [1]. *For any $c_0, c_1 \in \mathbb{R}$, a global minimizer of $MS(\cdot, c_0, c_1)$ can be found by carrying out the following minimization:*

$$\min_{0\leqslant u\leqslant 1} \int_\Omega |\nabla u|d\mathbf{x} + \int_\Omega \left[\lambda_0(I-c_0)^2 - \lambda_1(I-c_1)^2\right]u(\mathbf{x})d\mathbf{x}$$

and then setting $\Sigma = \{\mathbf{x} : u(\mathbf{x}) \geqslant \mu\}$ for a.e. $\mu \in [0,1]$.

2.2. Four phase model

Vese and Chan [5] extended the two-phase formulation to multi-phase case based on the observation that n level sets can be used to describe 2^n phases or regions. Here we restrict our description to the four phase model which is used in segmenting MR images effectively. Let $\phi_1, \phi_2 : \Omega \subset \mathbb{R}^2 \to \mathbb{R}$ be the two level sets. $H_1 = H(\phi_1), H_2 = H(\phi_2)$ and $\widetilde{H}_1 = 1 - H(\phi_1), \widetilde{H}_2 = 1 - H(\phi_2)$, representing four regions. Our goal is to solve a minimization problem

$$\min_{(\mathbf{c},\Phi)} F(\mathbf{c},\Phi) \quad (8)$$

with

$$F(\mathbf{c},\Phi) = \int_\Omega \delta(\phi_1)|\nabla\phi_1|d\mathbf{x} + \int_\Omega \delta(\phi_2)|\nabla\phi_2|d\mathbf{x} + \lambda_{11}\int_\Omega (I-c_{11})^2 H_1H_2d\mathbf{x} + \lambda_{10}\int_\Omega (I-c_{10})^2 H_1\widetilde{H}_2d\mathbf{x} + \lambda_{01}\int_\Omega (I-c_{01})^2\widetilde{H}_1H_2d\mathbf{x} + \lambda_{00}\int_\Omega (I-c_{00})^2\widetilde{H}_1\widetilde{H}_2d\mathbf{x}$$

where $\Phi = (\phi_1, \phi_2)$, and the constant mean values $\mathbf{c} = (c_{11}, c_{10}, c_{01}, c_{00})$ can be derived as

$$c_{11} = \frac{\int_\Omega IH_1H_2d\mathbf{x}}{\int_\Omega H_1H_2d\mathbf{x}}, \quad c_{10} = \frac{\int_\Omega IH_1\widetilde{H}_2d\mathbf{x}}{\int_\Omega H_1\widetilde{H}_2d\mathbf{x}}, \quad (9)$$

$$c_{01} = \frac{\int_\Omega I\widetilde{H}_1H_2d\mathbf{x}}{\int_\Omega \widetilde{H}_1H_2d\mathbf{x}}, \quad c_{00} = \frac{\int_\Omega I\widetilde{H}_1\widetilde{H}_2d\mathbf{x}}{\int_\Omega \widetilde{H}_1\widetilde{H}_2d\mathbf{x}}. \quad (10)$$

Note the zero level sets $\phi_i = 0, i = 1, 2$, represent object boundaries and the mean values $\mathbf{c}$ represent the expected average pixel values in these objects. Vese and Chan [5] used the corresponding gradient descent equations to implement the active contours [8]. In the numerical implementation of the above PDEs, a non-compactly supported, smooth approximation of the Heaviside function $H_\epsilon(\mathbf{x})$, such that $H_\epsilon(\mathbf{x}) \to H(\mathbf{x})$ as $\epsilon \to 0$ is utilized. Since the above minimization (8) is non-convex the time discretized gradient descent PDEs usually require large iterations and small time steps to convergence (typically in 100's of iterations). Moreover, the final segmentation result may not correspond to the global minimum of the energy function as the gradient descent scheme can be stuck at a local minima of the corresponding energy functional given in Eq. (8).

We note the corresponding gradient descent equations (time dependent Euler–Lagrange equations of Eq. (8)) for the level sets functions ϕ_1 and ϕ_2,

$$\phi_{1t} = \delta(\phi_1)\left(div\left(\frac{\nabla\phi_1}{|\nabla\phi_1|}\right) - r_1(\mathbf{c})\right) \quad (11)$$

and

$$\phi_{2t} = \delta(\phi_2)\left(div\left(\frac{\nabla\phi_2}{|\nabla\phi_2|}\right) - r_2(\mathbf{c})\right) \quad (12)$$

respectively. Here, the image fitting terms are given by,

$$r_1(\mathbf{c}) = (\lambda_{11}(I-c_{11})^2 - \lambda_{01}(I-c_{01})^2)H_2 + (\lambda_{10}(I-c_{10})^2 - \lambda_{00}(I-c_{00})^2)\widetilde{H}_2$$
$$r_2(\mathbf{c}) = (\lambda_{11}(I-c_{11})^2 - \lambda_{10}(I-c_{10})^2)H_1 + (\lambda_{01}(I-c_{01})^2 - \lambda_{00}(I-c_{00})^2)\widetilde{H}_1.$$

Following, Chan et al. [1], we drop the dirac delta functions ($\delta(\cdot)$ in (11) and (12)) allowing us to obtain the minimization

$$\min_{(\mathbf{c},\Phi)} \mathcal{F}(\mathbf{c},\Phi) \quad (13)$$

with

$$\mathcal{F}(\mathbf{c},\Phi) = \int_\Omega |\nabla\phi_1|d\mathbf{x} + \int_\Omega |\nabla\phi_2|d\mathbf{x} + \int_\Omega r_1(\mathbf{c})\phi_1d\mathbf{x} + \int_\Omega r_2(\mathbf{c})\phi_2d\mathbf{x}.$$

Then correspondingly we can derive an energy functional which does not depend on regularized Heaviside functions. Thus, we can solve the following globally convex energy minimization problem,

$$\min_{\mathbf{u}=(u_1,u_2)\in\{0,1\}^2} \mathcal{G}(\mathbf{c},\mathbf{u}) \quad (14)$$

with

$$\mathcal{G}(\mathbf{c},\mathbf{u}) = \int_\Omega |\nabla u_1|d\mathbf{x} + \int_\Omega |\nabla u_2|d\mathbf{x} + \lambda_{11}\int_\Omega (I-c_{11})^2u_1u_2d\mathbf{x} + \lambda_{01}\int_\Omega (I-c_{01})^2(1-u_1)u_2d\mathbf{x} + \lambda_{10}\int_\Omega (I-c_{10})^2u_1(1-u_2)d\mathbf{x} + \lambda_{00}\int_\Omega (I-c_{00})^2(1-u_1)(1-u_2)d\mathbf{x},$$

where Heaviside functions are replaced by $\mathbf{u} = (u_1, u_2) \in \{0,1\}^2$ which are known as *binary partitioning functions*. The above modified minimization problem (14) can further be relaxed to the set of functions $\mathbf{u} = (u_1, u_2) \in [0,1]^2$ in order to solve a convex

minimization problem. That is, the binary partitioning functions based energy minimization becomes,

$$\min_{\mathbf{u}=(u_1,u_2)\in[0,1]^2} \mathcal{G}(\mathbf{c},\mathbf{u}). \tag{15}$$

The following theorem provides the guarantee of finding a global minimizer for the derived functional (14) in terms of the relaxed version in (15). We follow arguments similar to the work of Chan et al. [1,36] to prove the following result.

Theorem 2. *For any $c_{11}, c_{10}, c_{01}, c_{00} \in \mathbb{R}$, a global minimizer for $\mathcal{G}(\mathbf{c},\cdot)$ in (14) can be found by carrying out the convex minimization problem (15).*

Proof. See Appendix A. □

The final segmentation is obtained by thresholding the functions u_1 and u_2 with any number in the interval $(0,1)$ for example at 0.5, as shown in Fig. 1b and c. Note that the above modified minimization model does not involve level sets and thus can be solved efficiently. Further, we can prove that the above relaxed minimization problem can be solved in a binary variable minimization formulation to find a global minimum. The existence of minimizers of the modified energy $\mathcal{G}$ given in Eq. (15) is proved using the theory of functions of bounded variation (BV) [56].

Theorem 3. *For a given input gray scale image $I \in L^\infty(\Omega)$, there exists a minimizer for the functional $\mathcal{G}$ in (15) in $\mathbb{R}^4 \times BV_{[0,1]}(\Omega)^2$.*

Proof. See Appendix B □

3. Experimental results

3.1. Implementation details

The four phase convex minimization problem in (15) is solved in an alternating fashion for the image variables (u_1, u_2):

$$\min_{u_j\in[0,1]} \left\{ \mathcal{G}_j(u_j) = \int_\Omega |\nabla u_j| d\mathbf{x} + \int_\Omega r_j(\mathbf{c}) u_j d\mathbf{x} \right\}. \tag{16}$$

where $j = 1, 2$ and the image region fitting terms are given by,

$$\begin{aligned} r_1(\mathbf{c}) &= (\lambda_{11}(I-c_{11})^2 - \lambda_{01}(I-c_{01})^2)u_2 \\ &+ (\lambda_{10}(I-c_{10})^2 - \lambda_{00}(I-c_{00})^2)(1-u_2), \\ r_2(\mathbf{c}) &= (\lambda_{11}(I-c_{11})^2 - \lambda_{10}(I-c_{10})^2)u_1 \\ &+ (\lambda_{01}(I-c_{01})^2 - \lambda_{00}(I-c_{00})^2)(1-u_1). \end{aligned}$$

Following [1], the constrained problem (16) is changed into an unconstrained minimization problem by solving

$$\min_{u_j\in[0,1]} \left\{ \mathcal{G}_j(u_j) = \int_\Omega |\nabla u_j| d\mathbf{x} + \int_\Omega (r_j(\mathbf{c}) u_j + \alpha_j v(u_j)) d\mathbf{x} \right\}, \tag{17}$$

where $v(\xi) := \max\{0, 2|\xi - \frac{1}{2}| - 1\}$ is an exact penalty function provided that $\alpha_j > \frac{1}{2}\|r_j\|_{L^\infty(\Omega)}$. Based on [42] we use a convex regularization of (17) involving the auxiliary variables (v_1, v_2) and solving the minimization problem

$$\min_{u_j,v_j} \left\{ \int_\Omega |\nabla u_j| d\mathbf{x} + \frac{1}{2\theta_j}\|u_j - v_j\|^2_{L^2(\Omega)} + \int_\Omega (r_j(\mathbf{c}) v_j + \alpha_j v(v_j)) d\mathbf{x} \right\}, \tag{18}$$

with θ_j chosen to be small [44] allowing us to split (18) into two minimization sub-problems with respect to u_j and v_j separately. To solve the convex optimization with respect u_j we use the Chambolle's dual formulation [43,42] of the total variation regularization function. In detail:

1. Solve for u_j:

$$\min_{u_j} \left\{ \int_\Omega |\nabla u_j| d\mathbf{x} + \frac{1}{2\theta_j}\|u_j - v_j\|^2_{L^2(\Omega)} \right\}. \tag{19}$$

The solution is given by

$$u_j = v_j - \theta_j div \mathbf{p}_j,$$

where the vector $\mathbf{p}_j = (p_{j_1}, p_{j_2})$ satisfies the equation

$$\nabla(\theta_j div \mathbf{p}_j - v_j) - |\nabla(\theta_j div \mathbf{p}_j - v_j)|\mathbf{p}_j = 0$$

and it is solved by a fixed point method: $\mathbf{p}_j^0 = 0$ and

$$\mathbf{p}_j^{n+1} = \frac{\mathbf{p}_j^n + \delta t \nabla(div(\mathbf{p}_j^n) - v_j/\theta_j)}{1 + \delta t|\nabla(div(\mathbf{p}_j^n) - v_j/\theta_j)|}. \tag{20}$$

We utilize the following stopping condition for the fixed point iterations,

$$\max_{\mathbf{x}\in\Omega}\{\mathbf{p}_j^{n+1}(\mathbf{x}) - \mathbf{p}_j^n(\mathbf{x})\} > tol \tag{21}$$

with the tolerance set at $tol = 10^{-2}$. That is, the criterion for stopping the iteration is to check that the maximum variation between the dual variables is less than the given tolerance.

2. Solve for the auxiliary variable v_j:

$$\min_{v_j} \left\{ \frac{1}{2\theta_j}\|u_j - v_j\|^2_{L^2(\Omega)} + \int_\Omega (r_j(\mathbf{c}) v_j + \alpha_j v(v_j)) d\mathbf{x} \right\}, \tag{22}$$

for which the solution is given by:

$$v_j = \min\{\max(u_j(\mathbf{x}) - \theta_j r_j(\mathbf{c}), 0), 1\}.$$

Furthermore, at every few iterations (set at 10 iterations, see Fig. 4 and Section 3.3) the vector $\mathbf{c}$ is updated according to the following equations:

$$c_{11} = \frac{\int_\Omega I u_1 u_2 d\mathbf{x}}{\int_\Omega u_1 u_2 d\mathbf{x}}, \quad c_{10} = \frac{\int_\Omega I u_1 (1-u_2) d\mathbf{x}}{\int_\Omega u_1 (1-u_2) d\mathbf{x}}, \tag{23}$$

$$c_{01} = \frac{\int_\Omega I (1-u_1) u_2 d\mathbf{x}}{\int_\Omega (1-u_1) u_2 d\mathbf{x}}, \quad c_{00} = \frac{\int_\Omega I (1-u_1)(1-u_2) d\mathbf{x}}{\int_\Omega (1-u_1)(1-u_2) d\mathbf{x}}. \tag{24}$$

The computation of $\mathbf{c}$ values are similar to the ones in Vese and Chan model [5] (see Eqs. (9) and (10)) except that they are now based on the binary partitioning functions and does not involve computing regularized Heaviside functions. We refer to [43] for more details on this particular form of dual minimization and the motivation for the fixed point method used to derive the solution for the auxiliary variable in the second step.

3.2. Datasets and parameters

We have used some real MR images from the atlas of normal structure and blood flow from the Whole Brain Atlas website.[1] The images presented here are from T1 MRI imaging modality with slice thickness of 1 mm. We also utilize the full brain MRI images available at the BrainWeb database[2] which allows us to experiment with synthetically generated noise (calculated relative to the brightest tissue, and denoted by "*n*") and intensity non-uniformity (denoted by "*RF*") to test the robustness of our scheme. BrainWeb is a simulated brain database which contains a set of realistic MRI data volumes produced by a powerful MR simulator. This database

[1] http://www.med.harvard.edu/aanlib/home.html.
[2] http://brainweb.bic.mni.mcgill.ca/brainweb/.

is widely used by the neuroimaging community to evaluate the performance of various image analysis methods [57].

The parameters $\theta_1 = \theta_2 = 0.001$ were fixed for the segmentation results reported here. We observed that decreasing the θ's increased the speed of convergence. In order to simplify notations we use $\lambda = \lambda_{11} = \lambda_{01} = \lambda_{10} = \lambda_{00}$ and we fix $\lambda = 1$ in all our experiments reported here. Equal weights (λ_{ij}'s) are used for the four regions to be segmented as we do not want to introduce bias for certain phases and it worked for the brain MRI datasets we used here. The time step parameter $\delta t = 1/8$ for the fixed point iterations (20) (which typically converged in $n = 5$ iterations) with tolerance 10^{-2} in (21) is used. We note that these optimal parameters were set for both the brain MRI datasets used here which obtained best segmentation results (see Section 3.4) and no further tuning is necessary. Our scheme takes less than 0.2 s (for 100 iterations) on MATLAB2012a on a Mac laptop with Intel Core i7 CPU 2.3 GHz, 8 GB RAM CPU. Meanwhile, the average computation time for related models compared from the literature are in the region of 30 s (for 100 iterations as an upper bound) to converge to the final segmentation.

3.3. Example segmentations

Fig. 2 shows an example segmentation result of our globally convex four phase scheme on a normal brain MRI transaxial slice from the Whole Brain Atlas, see also Fig. 1 where we show a coronal slice from the same atlas. Fig. 2b and c show the two functions u_1, u_2 computed using our scheme and thresholded at 0.5 respectively. As can be seen, the binary function from u_1, corresponding to level set ϕ_1, contains *gray matter* (Fig. 2b, $u_1 > 0.5$, shown in white color) whereas *white matter* ($u_1 < 0.5$, shown in black color) is combined with the background. Similarly the binary function

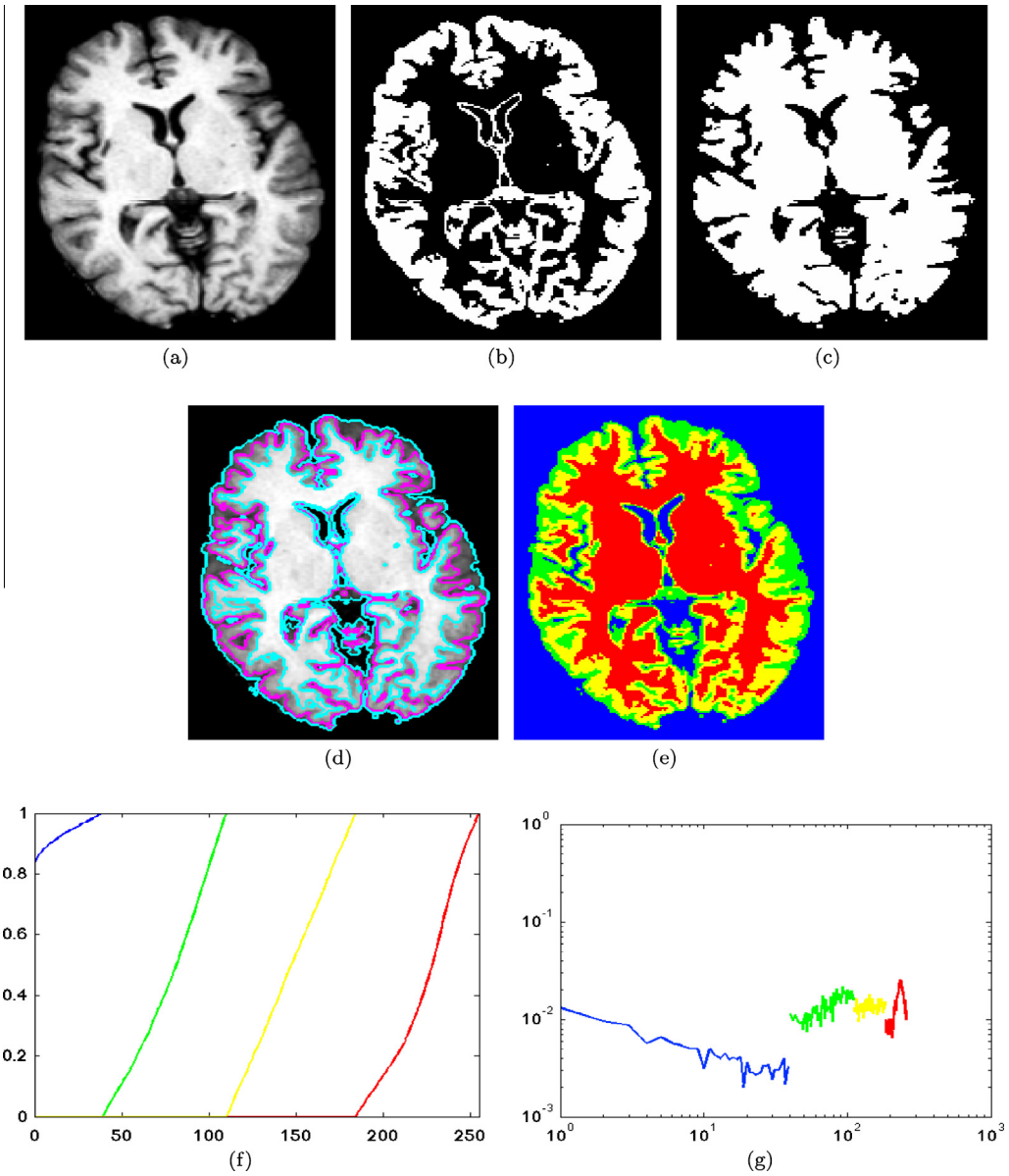

Fig. 2. Our fast four phase image segmentation model provides good segmentation results by distinguishes different tissue classes. (a) Input image, transaxial slice from a normal brain MR imagery. (b) Final binary segmentation from u_1. (c) Final binary segmentation from u_2. (d) Segmentation result showing the contours superimposed on the input image, with $\lambda = 1$. (e) Color visualization of the segmentation result showing four different regions. (f) Cumulative distribution function (CDF) of the four regions from (e). (g) Histogram (log-scaled) of the four regions showing the separation clearly. (For interpretation of the references to color in this figure legend, the reader is referred to the web version of this article.)

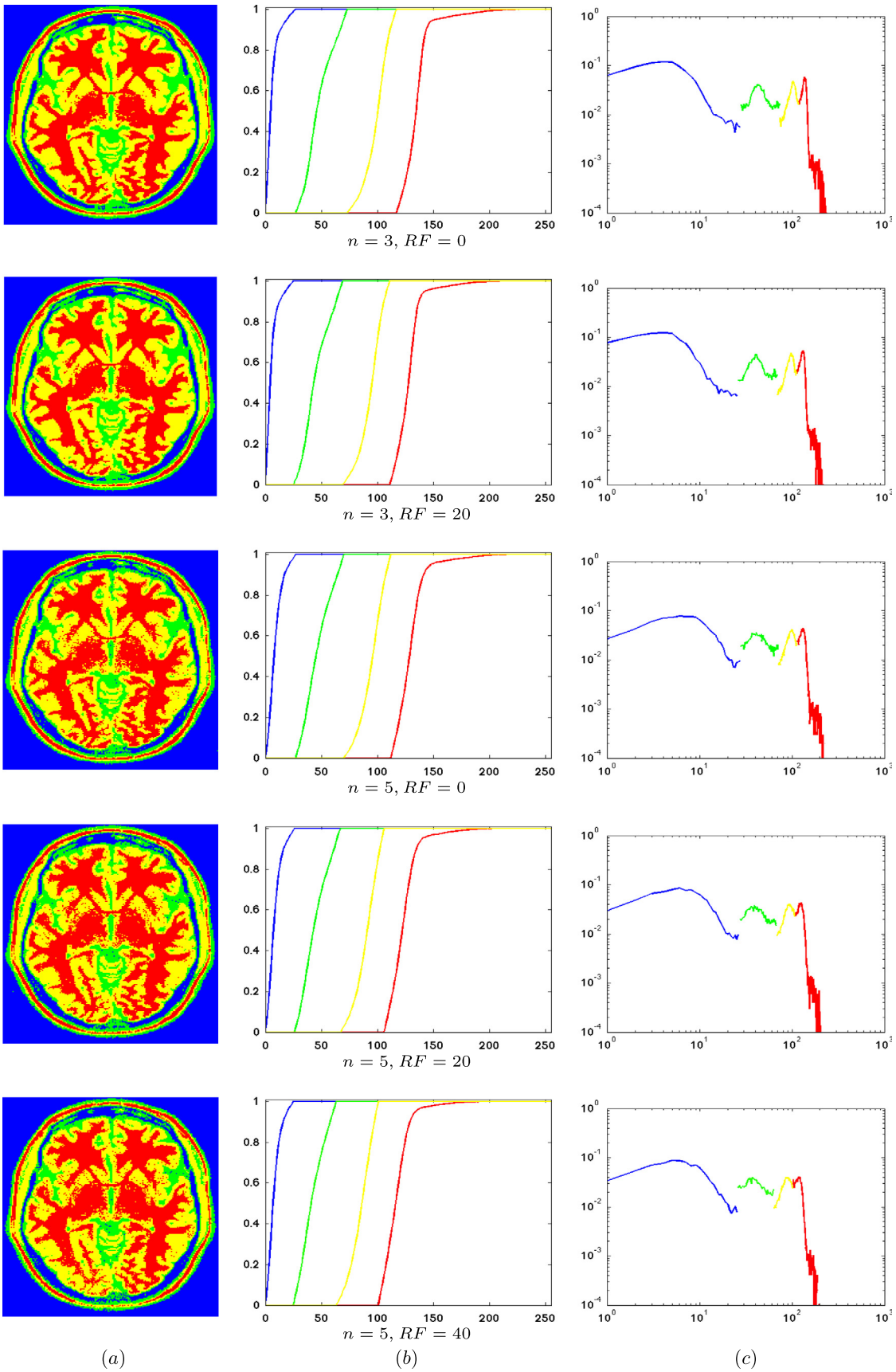

Fig. 3. Robustness of our multiphase scheme with respect to noise (n) and non-uniformity (RF). (a) Color visualization of the segmentation results. (b) CDF of regions. (c) Log-scaled histograms. (For interpretation of the references to color in this figure legend, the reader is referred to the web version of this article.)

from u_2, corresponding to level set ϕ_2, contains *muscle* (Fig. 2(c), $u_1 > 0.5$, shown in white color) whereas *background* ($u_2 < 0.5$, shown in black color) is combined with *Cerebrospinal fluid (CSF)*. In order to discern the background and CSF, we need to look at the intersection regions of the functions u_1 and u_2. For this purpose we show the result of our four phase model as contours corresponding to the threshold regions $\{\mathbf{x} \in \Omega : u_1(\mathbf{x}) = 0.5\}$, and $\{\mathbf{x} \in \Omega : u_2(\mathbf{x}) = 0.5\}$, see Fig. 2d where two contours (Cyan, Magenta) are overlaid on top of the input image. In Fig. 2e we use four different colors (Blue, Green, Yellow, and Maroon) which highlight different phases for better visualization of phase separation and boundary detection of regions. In Fig. 2f and g, we show cumulative distribution function (CDF) and the histogram of each of the four regions computed by the proposed method. The histograms highlight separation of different phases/regions indicating the superior performance of our splitting based numerical approach.

Fig. 3 shows segmentation results for an MR image (Slice 67 from the BrainWeb synthetic atlas) to show the robustness of our scheme with respect to various amount of noise and intensity non-uniformity. We change the amount of noise n from 3% to 5% and intensity non-uniformity *RF* from 0 to 40. As can be seen from the final segmentation results in Fig. 3 (left column), we obtain stable segments under different *RF* (Fig. 3 top two rows) and when the noise increases the segmentation results remain stable (Fig. 3 bottom three rows). Next, Fig. 4 shows the corresponding energy values (15) against iterations with different number updates for the constant $\mathbf{c} = (c_{11}, c_{10}, c_{01}, c_{00})$ in Eqs. (23) and (24) in our

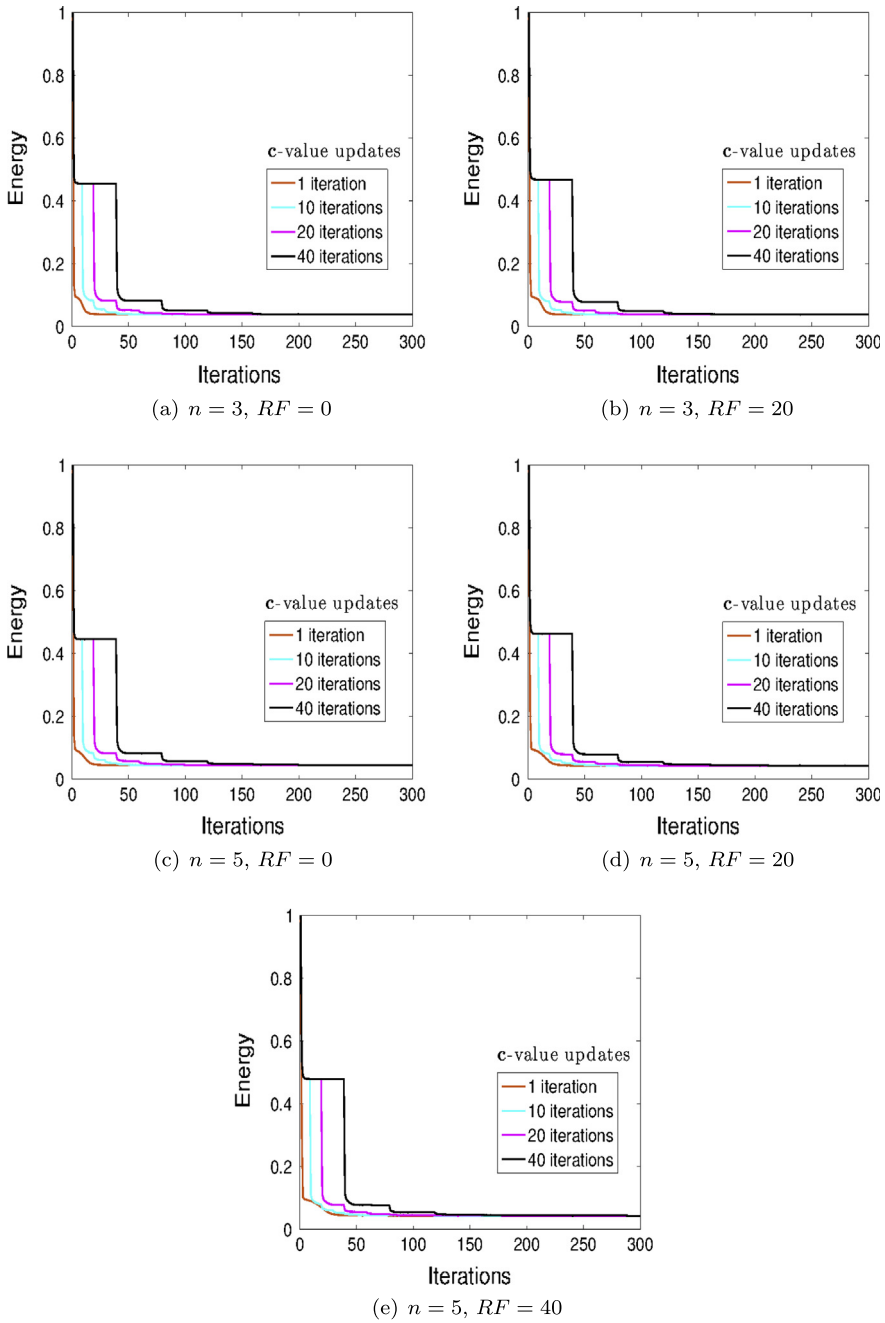

Fig. 4. Iterations versus normalized energy for different number of update iterations for the vector **c** (23) and (24). We show for different noise (n) and intensity non-uniformity (*RF*) values corresponding to the Fig. 3.

implementation. As can be seen, updating the constant at every iteration decreases the energy rapidly initially and keeps it near zero (but not zero) whereas updating at every 40 iterations decreases in a piecewise manner but with large drop in energy values as the increase the iterations. We chose to update the **c** at every 10 iterations in our alternating minimization implementation (15). Thus we see that updating the mean values **c** computed using Eqs. (23) and (24) at only few iterations does not necessarily increase the speed of convergence. Further analysis of the implementation presented in Section 3.1 and obtaining convergence rates are open research questions which needs to be explored further.

Fig. 5 shows representative segmentation results for full brain BrainWeb data-set (transaxial slices are shown) with different noise ("*n*") and non-uniformity ("*RF*") levels for our scheme. Different *n* and *RF* are specified in Fig. 5 for each row. This illustrates that our scheme preserves topological changes as we move through the image stack as well as our scheme can handle noise and intensity non-uniformity together effectively.

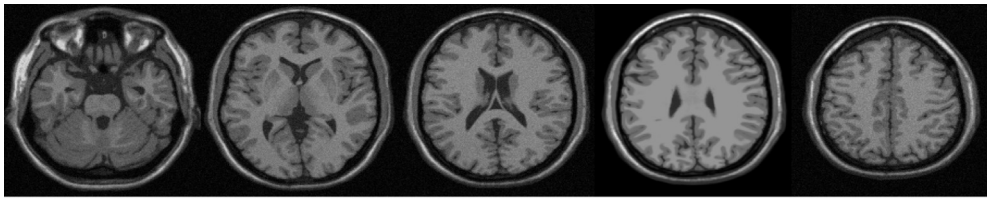

Noise-free brain MRI images

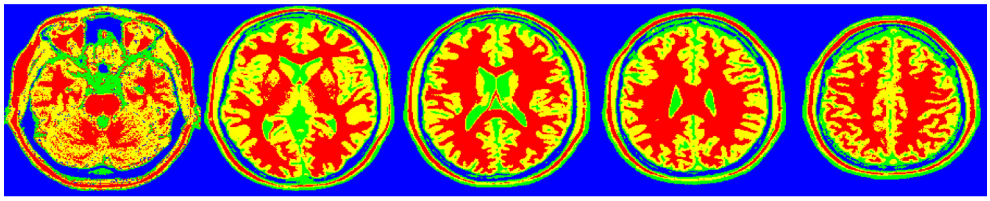

$n = 3,\ RF = 0$

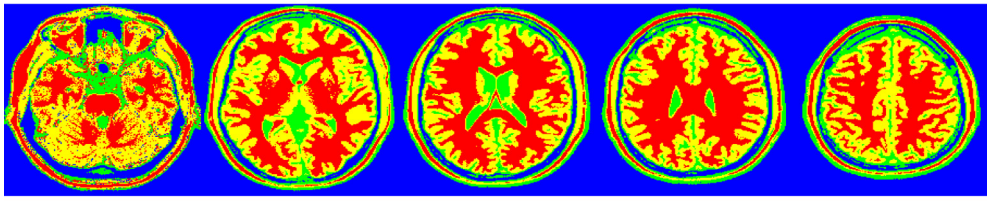

$n = 3,\ RF = 20$

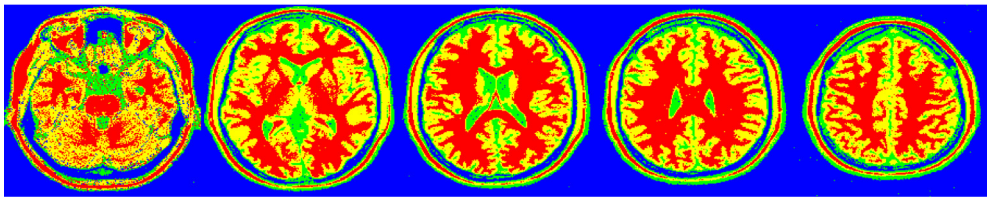

$n = 5,\ RF = 0$

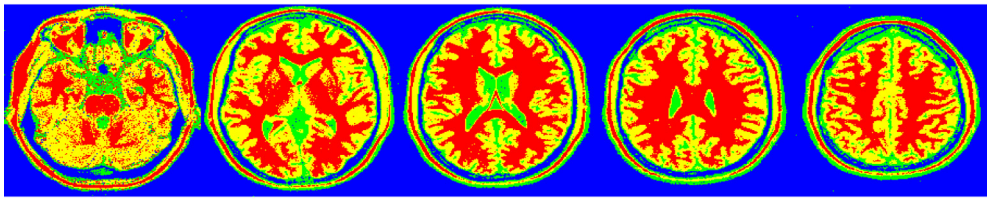

$n = 5,\ RF = 20$

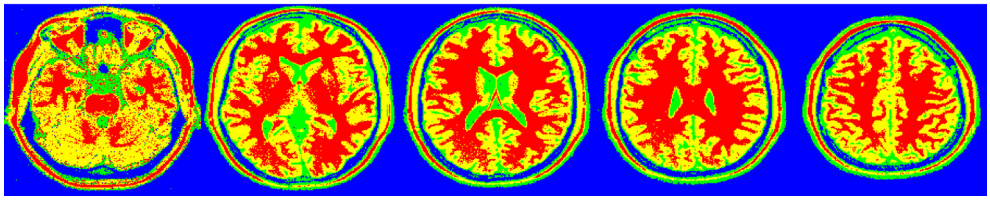

$n = 5,\ RF = 40$

Fig. 5. Our four phase segmentation results for full brain data-sets with representative transaxial slices. First row shows the noise-free brain MRI images. Next subfigures present segmentation results for different noise (*n*) and non-uniformity (*RF*) values for our scheme. Segmentation results remain stable for increasing values of noise and intensity inhomegenities.

3.4. Comparison results

Fig. 6 shows a comparison result with other related multiphase active contour methods which we describe briefly and refer the reader to the corresponding references for more details.

- *Ker* [46]: This method implements a kernel function which maps implicitly the original image data into data of a higher dimension and uses level set algorithm for multiphase segmentation.
- *Mean* [5]: Classical Vese–Chan multiphase piecewise constant model implemented using the level set algorithm.
- *Clust* [47]: This method uses curve evolution equations along with a partition constraint which uses the rule that if a point leaves a region then it is claimed by a single other region.
- *Primal–Dual* [48]: This uses a primal–dual minimization method for the piecewise constant multiphase active contour scheme.

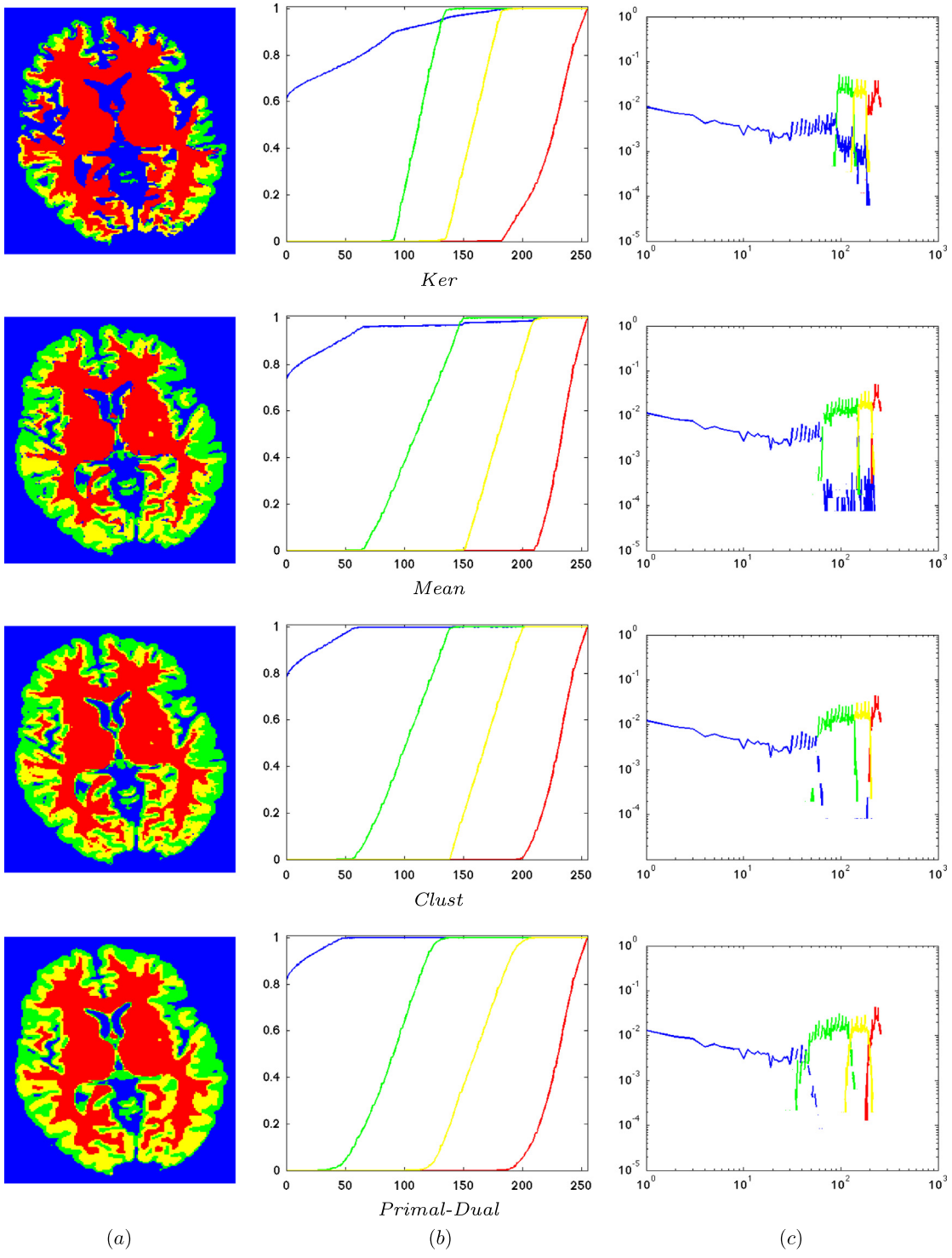

Fig. 6. Comparison with *Ker, Mean, Cluster, Mean, Primal–Dual* multiphase segmentation methods. (a) Color coded visualization of the obtained segmentation result. (b) Cumulative distribution function (CDF) of the four computed regions. (c) Histogram (log-scaled) of the four regions showing the intersections. (For interpretation of the references to color in this figure legend, the reader is referred to the web version of this article.)

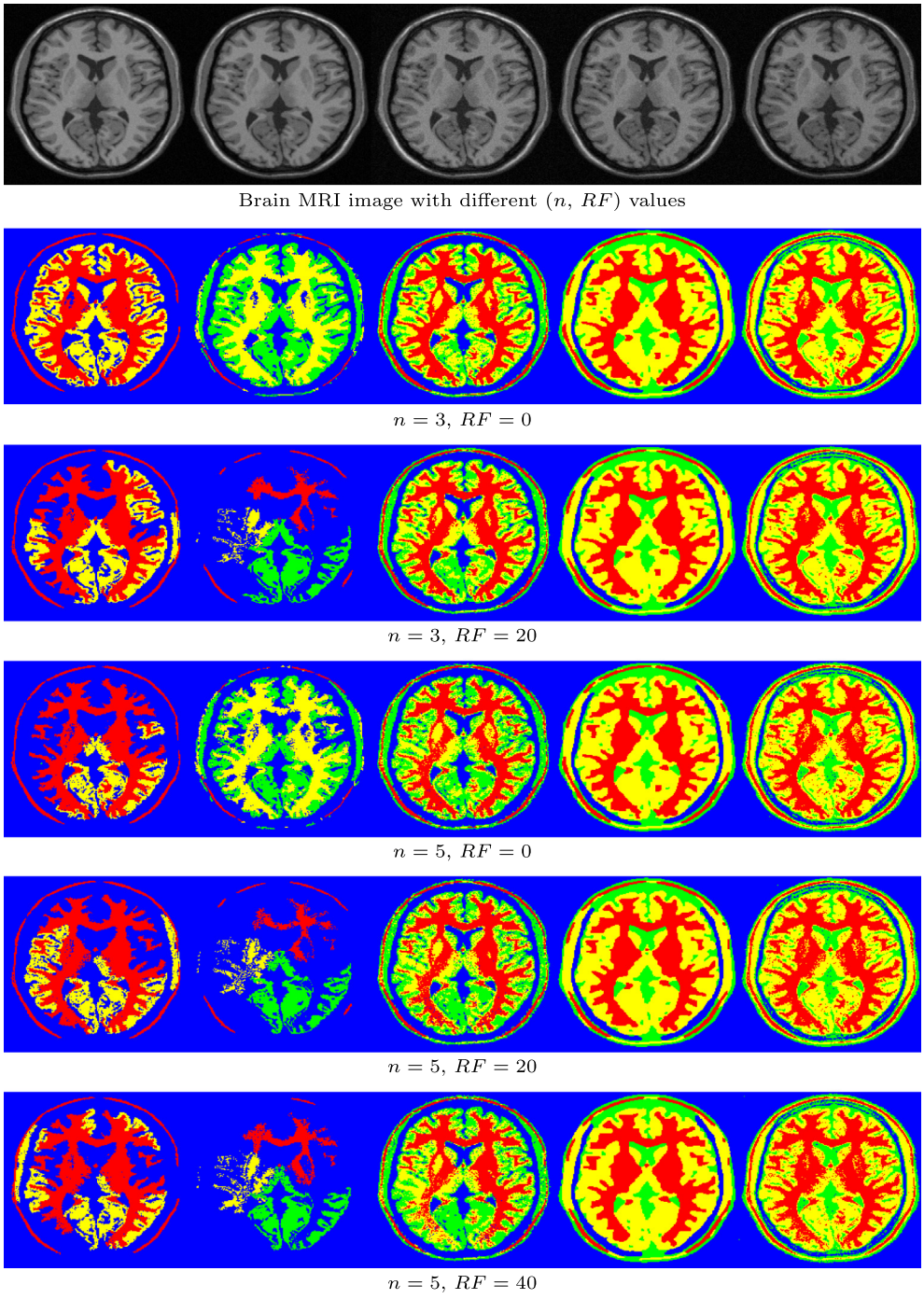

Fig. 7. Comparison of different schemes for a single brain MRI image (Slice number 79) for different noise (n) and non-uniformity (RF) values. The top subfigure is different input images. Remaining subfigures contain different segmentation results. From second to sixth row: *Ker, Mean, Clust, Primal–dual*, and Our approach, respectively.

We utilize the same real MR image given in Fig. 2a for comparing other schemes. In Fig. 6b and c we show CDFs and histograms computed for each of the computed phases respectively. Compared with the histograms shown in Fig. 2f and g for our scheme, we see that the proposed model provides better separation of regions. The histograms for the other schemes in Fig. 6c show nontrivial intersections, highlighting the drawback in using level set based implementations. Moreover, the noise remains as speckles in the segmented regions whereas our model handles it efficiently.

Finally, in Fig. 7 we show different segmentation results for a particular image (slice number 79) taken across all noise and inhomogeneity levels for different schemes. The results indicate that *Ker* and *Mean* methods can lead to poor separation of different regions whereas noise can affect the result of *Clust* and *Primal–Dual* schemes. Meanwhile, our approach performs well and handles higher non-uniformity without degrading the final segmentation results. Further data-sets and extensive comparison results of all the schemes for full brain stacks are available online.[3]

We further use the following quantitative error metrics to compare the schemes with gold standard ground truth segmentations

[3] http://cell.missouri.edu/pages/BrainMRISegmentation.

on BrainWeb synthetic atlas with different noise and intensity non-uniformity values. For more details about objective evaluation of image segmentation algorithms and for precise definitions of these metrics we refer to [58].

- *DICE*:
  The Dice coefficient [59] is a popular error metric and it is used to compare ground truth segmentation with those obtained with automatic multiphase segmentation schemes. By definition, for two binary segmentations A and B, the Dice coefficient is computed as:

$$D(A,B) = \frac{2|A \cap B|}{|A| + |B|}. \tag{25}$$

Here the binary segmentation is computed automatically, using the segmentation curves and by thresholding regions obtained by all algorithms. The notation $|A|$ denotes the number of pixels in the set A. Note that, a D value of 1 indicates perfect agreement. In particular, higher numbers indicate that the results of that particular scheme's result match the gold standard better than results that produce lower Dice coefficients.

- *RI*:
  Rand index: A metric based on a classical nonparametric test and is computed by counting pairs of pixels that have compatible label relationships in the two segmentations to be compared. Values closer to 1 indicate better segmentation result.
- *GCE*:
  Global consistency error: A metric which computes the degree of overlap of the cluster associated with each pixel in one segmentation and its ÒclosestÓ approximation in the other segmentation. Values closer to 0 indicate better segmentation results.
- *VI*:
  Variation of information: A metric related to the conditional entropies between the class label distribution of the segmentations. This computes a measure of information content in each of the segmentations and how much information one segmentation gives about the other. Lower values indicate better segmentation results.

Note that all these metrics are for comparing two segmentations, one of which is assumed to be the available ground truth. Table 1 shows the comparison of average Dice values (for a total

Table 1
Average Dice coefficients values for different schemes in four different phases (regions). Values near 1 indicate the closeness of the segmentation to the ground truth segmentation. Best results are indicated by boldface.

n	*RF*	Regions	*Ker*	*Mean*	*Clust*	*Primal–Dual*	*Our*
3	0	D1	0.305670	0.824283	0.886665	0.698128	**0.944007**
		D2	0.224586	0.581326	0.419365	0.700223	**0.915818**
		D3	0.131252	0.363182	0.110626	0.718244	**0.870375**
		D4	0.565510	0.840712	0.693652	0.955584	**0.965933**
3	20	D1	0.306836	0.767452	0.873386	0.692621	**0.931111**
		D2	0.223917	0.534288	0.432176	0.695534	**0.907063**
		D3	0.130171	0.303436	0.110716	0.718225	**0.873175**
		D4	0.563268	0.823805	0.645526	0.953754	**0.967594**
5	0	D1	0.305627	0.788663	0.877971	0.688774	**0.912402**
		D2	0.226171	0.539260	0.311053	0.680036	**0.879323**
		D3	0.126738	0.299720	0.100588	0.688052	**0.829607**
		D4	0.544178	0.807202	0.669333	0.948687	**0.954868**
5	20	D1	0.309830	0.746360	0.866684	0.708890	**0.903028**
		D2	0.225578	0.510120	0.318350	0.685553	**0.870886**
		D3	0.132034	0.253848	0.111433	0.683057	**0.824065**
		D4	0.539861	0.780266	0.613947	0.944511	**0.953657**
5	40	D1	0.310085	0.715360	0.825330	0.685356	**0.872111**
		D2	0.226430	0.478908	0.286386	0.678544	**0.844355**
		D3	0.130849	0.221841	0.127278	0.670710	**0.806790**
		D4	0.542354	0.766757	0.586870	0.543010	**0.951143**

Table 2
Average Rand Index (RI), Global Consistency Error (GCE) and Variation of Information (VI) for different schemes. Best results are indicated by boldface.

n	RF	Error metrics	Ker	Mean	Clust	Primal–Dual	Our
3	0	RI	0.527025	0.849013	0.672026	0.895372	**0.946341**
		GCE	0.332322	0.223942	0.158767	0.173467	**0.085668**
		VI	2.483764	1.177137	1.490298	0.992642	**0.569099**
3	20	RI	0.525251	0.833570	0.659371	0.887008	**0.941475**
		GCE	0.329012	0.236016	0.171285	0.189292	**0.096797**
		VI	2.477927	1.255048	1.564992	1.065011	**0.620833**
5	0	RI	0.523815	0.825506	0.648725	0.884315	**0.921506**
		GCE	0.333999	0.250001	0.154166	0.194308	**0.135605**
		VI	2.507981	1.326232	1.563033	1.087131	**0.828043**
5	20	RI	0.522536	0.813937	0.629603	0.877183	**0.917244**
		GCE	0.330010	0.252157	0.166120	0.209219	**0.142290**
		VI	2.495524	1.375133	1.642941	1.148695	**0.858660**
5	40	RI	0.520192	0.805794	0.604564	0.865636	**0.905678**
		GCE	0.326658	0.256492	0.176804	0.231084	**0.163501**
		VI	2.489061	1.423080	1.737919	1.240130	**0.950309**

of 181 images) of different models for different noise and intensity inhomogenieties taken from BrainWeb database. As can be seen, our scheme performs better in terms of the Dice coefficient compared with other related approaches for all noise levels in all the four regions. Similarly in Table 2 we see that the average value of metrics RI, GCE and VI for different schemes against our model shows that the proposed globally convex multiphase scheme performs well overall.

4. Conclusion and discussion

We considered a fast globally convex four phase active contour scheme for MRI image segmentation inspired by Chan et al. [1] approach and provide a well-posed convex energy minimization which can be used to determine piecewise constant segmentations without level sets. By using a dual minimization-based implementation our approach provides better phase differentiation than other schemes. Experimental results on brain MRI images indicate the proposed approach provides better results compared with other active contour based multiphase segmentation schemes.

The four phase method we studied is found to provide better phase separation which is relevant in biomedical imagery. Experimental results indicate that our method performs better than other multiphase schemes which are applied MR image segmentation in terms of different error metrics. We obtain better differentiation of gray, white matters and the background in an unsupervised manner. Further, finer differentiation of other tissue classes such as CSF, fat, muscle, blood vessels, connective tissue (region around fat), dura matter and bone marrow will require more features and adaptive choice of parameters used in our implementation. This requires prior anatomical knowledge about the tissues which then can be used to pick our parameters for obtaining finer segmentations. The methodology presented here is general and currently we are developing the method to work for different imaging modalities (for example natural images from the Berkeley segmentation dataset [55], and biomedical images [54]). Our preliminary analysis suggest that we need to incorporate further features (color, texture, motion) before it can be applied for such images.

The main theoretical results we proved assume that the mean values are known a priori. Relaxing this assumption and proving the convergence of dual minimization based alternating iterative scheme are open though the numerical results indicate our approach works well for MR image segmentation. We also remark that the L^2-norm can be replaced by L^1-norm as a fidelity measures being particularly suitable for handling non-Gaussian additive noise and it will not erode geometric structures of the image during the segmentation allowing to preserve the contrast [60,42,61]. Currently we are developing a completely convex formulation of the original multiphase Vese and Chan model to guarantee the existence of a global solution when the constant values for each phase are not known a prior as well. Further, we plan to extend the multiphase model to perform surface segmentations from 3D MRI images similar to [9] as well as a method to extract intensity non-uniformity patterns coupled with segmentations [17].

Appendix A. Equivalence between (14) and (15) minimizations

Proof (*Proof of Theorem 2*). We use the standard notation for functions of bounded variation [62]. Since $\mathbf{u} \in [0,1]^2$, it follows from the standard total variation based Coarea Formula (see Theorem 4 below),

$$\int_\Omega |\nabla u_1| d\mathbf{x} = \int_0^1 \int_0^1 Per(\{\mathbf{x} \in \Omega : u_1(\mathbf{x}) > \zeta_1\}) d\zeta_1 d\zeta_2,$$

and

$$\int_\Omega |\nabla u_2| d\mathbf{x} = \int_0^1 \int_0^1 Per(\{\mathbf{x} \in \Omega : u_2(\mathbf{x}) > \zeta_2\}) d\zeta_1 d\zeta_2.$$

For the image fitting term,

$$\begin{aligned}\int_\Omega (u-c_{11})^2 u_1 u_2 d\mathbf{x} &= \int_\Omega (u-c_{11})^2 \prod_{i=1}^{2} \left(\int_0^1 \mathbb{1}_{\{\mathbf{x}\in\Omega: u_i > \zeta_i\}} d\zeta_i \right) d\mathbf{x} \\ &= \int_0^1 \int_0^1 \int_\Omega (u-c_{11})^2 \mathbb{1}_{\{\mathbf{x}\in\Omega: u_1>\zeta_1\}} \mathbb{1}_{\{\mathbf{x}\in\Omega: u_2>\zeta_2\}} d\mathbf{x} d\zeta_1 d\zeta_2.\end{aligned}$$

Further similar computations yield,

$$\int_\Omega (u-c_{01})^2 (1-u_1) u_2 d\mathbf{x} = \int_0^1 \int_0^1 \int_\Omega (u-c_{01})^2 (1-\mathbb{1}_{\{\mathbf{x}\in\Omega: u_1>\zeta_1\}}) \mathbb{1}_{\{\mathbf{x}\in\Omega: u_2>\zeta_2\}} d\mathbf{x} d\zeta_1 d\zeta_2,$$

$$\int_\Omega (u-c_{10})^2 u_1 (1-u_2) d\mathbf{x} = \int_0^1 \int_0^1 \int_\Omega (u-c_{10})^2 \mathbb{1}_{\{\mathbf{x}\in\Omega: u_1>\zeta_1\}} (1-\mathbb{1}_{\{\mathbf{x}\in\Omega: u_2>\zeta_2\}}) d\mathbf{x} d\zeta_1 d\zeta_2,$$

$$\int_\Omega (u-c_{00})^2 (1-u_1)(1-u_2) d\mathbf{x} = \int_0^1 \int_0^1 \int_\Omega (u-c_{00})^2 (1-\mathbb{1}_{\{\mathbf{x}\in\Omega: u_1>\zeta_1\}})(1-\mathbb{1}_{\{\mathbf{x}\in\Omega: u_2>\zeta_2\}}) d\mathbf{x} d\zeta_1 d\zeta_2.$$

Defining $\mathbb{1}_{\mathbf{u}} := (\mathbb{1}_{\{\mathbf{x}\in\Omega: u_1>\zeta_1\}}, \mathbb{1}_{\{\mathbf{x}\in\Omega: u_2>\zeta_2\}})$, it follows that

$$\mathcal{G}(\mathbf{c}, \mathbf{u}) = \int_0^1 \int_0^1 \mathcal{G}(\mathbf{c}, \mathbb{1}_{\mathbf{u}}) d\zeta_1 d\zeta_2 = \int_0^1 \int_0^1 F(\mathbf{c}, \mathbf{u} - \boldsymbol{\zeta}) d\zeta_1 d\zeta_2,$$

for *a.e.* $\boldsymbol{\zeta} = (\zeta_1, \zeta_2) \in [0,1]^2$. Thus, it follows from the above equations that if $\mathbf{u}$ is a minimizer of the convex relaxed problem (15), then for *a.e.* $\boldsymbol{\zeta} \in [0,1]^2$, the function $\mathbf{w}_1 = \mathbb{1}_{\mathbf{u}}$ is a minimizer of the problem (14). □

Remark 1. Note also that $\mathbf{w}_2 = \mathbf{u} - \boldsymbol{\zeta}$ is a solution of the original Vese and Chan minimization problem (8). This shows that the relaxed convex minimization problem is equivalent to the original Vese and Chan piecewise constant multiphase formulation (8), we refer to Chan et al. [1] for more details.

We note that the Theorem 2 assumes the constants $\mathbf{c} = (c_{11}, c_{10}, c_{01}, c_{00})$ to be known to obtain a global minimizer of the energy minimization problem (15). In the image segmentation problem, we assume that these constants are unknown and they are part of the minimization problem considered in our implementation (see Section 3.1, we update the constants $\mathbf{c}$ in Eqs. (23) and (24) at every few iterations). Currently there are no results which can guarantee that the alternating minimization scheme for both the image functions and constants, that is for $(u_1, u_2, \mathbf{c})$, converges to the global minimum of (15). Nevertheless we observed numerically that the proposed implementation decrease the energy value rapidly, see Fig. 4.

Appendix B. Existence results

In order to prove the existence of a solution to our problem in (15) we need to recall a definition and some properties of functions of bounded variation [62,63].

Definition 1. Let $\Omega \subset \mathbb{R}^n$ be an open set and $u \in L^1(\Omega)$. The total variation of u in Ω is defined by

$$\int_\Omega |\nabla u| d\mathbf{x} := \sup_{\boldsymbol{\phi} \in \Phi} \left\{ \int_\Omega u div \boldsymbol{\phi} d\mathbf{x} \right\},$$

where $\Phi = \left\{ \boldsymbol{\phi} \in C_0^1(\Omega, \mathbb{R}^n) : |\boldsymbol{\phi}(\mathbf{x})| \leqslant 1 \text{ in } \Omega \right\}$.

Definition 2. $u \in L^1(\Omega)$ is a function of bounded variation if $\int_\Omega |\nabla u| d\mathbf{x}$ is finite. $BV(\Omega)$ is the space of all functions in $L^1(\Omega)$ with bounded variation. The $BV(\Omega)$ space is endowed with the norm $\|u\|_{BV(\Omega)} = \|u\|_{L^1(\Omega)} + \int_\Omega |\nabla u| d\mathbf{x}$, which makes it a Banach space. The set of functions $u \in BV(\Omega)$ taking values in $[0,1]$ is denoted by $BV_{[0,1]}(\Omega)$.

Definition 3. A Borel subset $E \subseteq \Omega$ is called a set of finite perimeter in Ω, when the associated characteristic function, $\mathbb{1}_E$, belongs to $BV(\Omega)$. The perimeter of E in Ω is defined as $Per(E) := \int_\Omega |\nabla \mathbb{1}_E| d\mathbf{x}$.

Theorem 4 (*Coarea Formula*). *If $u \in BV(\Omega)$, then for a.e. $t \in \mathbb{R}$, the level set $E_t := \{\mathbf{x} \in \Omega : u(\mathbf{x}) > t\}$ has finite perimeter, i.e., the characteristic function $\mathbb{1}_{E_t} \in BV(\Omega)$. Then, one has*

$$\int_\Omega |\nabla u| d\mathbf{x} = \int_{-\infty}^{\infty} Per(E_t) dt.$$

Theorem 5 (*Compactness*). *Let Ω be a 1-regular open bounded subset of $\mathbb{R}^n$. Then, for all p such that $1 \leqslant p < \frac{n}{n-1}$, the embedding $BV(\Omega) \subset L^p(\Omega)$ is compact.*

Theorem 6 (*Lower Semicontinuity*). *Let $(u^k)_{k\in\mathbb{N}}$ be a sequence in $BV(\Omega)$ strongly converging to some $u \in L^1(\Omega)$ and satisfying $\sup_{k\in\mathbb{N}} \int_\Omega |\nabla u^k| d\mathbf{x} < +\infty$. Then, $u \in BV(\Omega)$, $\int_\Omega |\nabla u| d\mathbf{x} \leqslant \liminf_{k\to+\infty} \int_\Omega |\nabla u^k| d\mathbf{x}$, and u^k weakly converges to u in $BV(\Omega)$.*

We are now ready to prove our main result.

Proof of Theorem 3. Let $m := \inf \mathcal{G}(\mathbf{c}, \mathbf{u})$ and $\{(\mathbf{c}^k, \mathbf{u}^k)\}_{k=1}^{\infty} \subseteq \mathbb{R}^4 \times BV_{[0,1]}(\Omega)^2$ be a minimizer sequence for the energy $\mathcal{G}$, i.e.,

$$\mathcal{G}(\mathbf{c}^k, \mathbf{u}^k) \overset{k\to\infty}{\to} m.$$

Since $\{\mathbf{u}^k\}_{k=1}^{\infty}$ is bounded in $BV_{[0,1]}(\Omega)^2$, there is a subsequence also denoted by $\{\mathbf{u}^k\}_{k=1}^{\infty}$, strongly convergent to an element $\mathbf{u}^* \in L^1(\Omega)^2$ (Theorem 5). Furthermore, $\mathbf{u}^* \in L^1_{[0,1]}(\Omega)^2$. Therefore, it follows that $\mathbf{u}^* \in BV_{[0,1]}(\Omega)^2$ and

$$\int_\Omega |Du_i^*| d\mathbf{x} \leqslant \liminf_{k\to\infty} \int_\Omega |Du_i^k| d\mathbf{x} \quad (\text{with } i = 1,2) \tag{B.1}$$

(Theorem 6). Now, considering $\mathcal{G}$ as a function of $\mathbf{c}$, its minimization brings the following two equations,

$$c_{11}^k = \frac{\int_\Omega I u_1^k u_2^k d\mathbf{x}}{\int_\Omega u_1^k u_2^k d\mathbf{x}}, \quad c_{10}^k = \frac{\int_\Omega I u_1^k (1-u_2^k) d\mathbf{x}}{\int_\Omega u_1^k (1-u_2^k) d\mathbf{x}}$$
$$c_{01}^k = \frac{\int_\Omega I (1-u_1^k) u_2^k d\mathbf{x}}{\int_\Omega (1-u_1^k) u_2^k d\mathbf{x}}, c_{00}^k = \frac{\int_\Omega I (1-u_1^k)(1-u_2^k) d\mathbf{x}}{\int_\Omega (1-u_1^k)(1-u_2^k) d\mathbf{x}}.$$

Since $I \in L^\infty(\Omega)$, it follows $\{\mathbf{c}^k\}_{k=1}^{\infty}$ is uniformly bounded. Hence, there is a subsequence also denoted by $\{\mathbf{c}^k\}_{k=1}^{\infty} \subset \mathbb{R}^{2n}$ and a constant vector $\mathbf{c}^* \in \mathbb{R}^{2n}$ such that

$$\mathbf{c}^k \overset{k\to\infty}{\to} \mathbf{c}^*.$$

Then, from Fatou's lemma we get for the suitable sequence $\{(\mathbf{c}^k, \mathbf{u}^k)\}_{k=1}^{\infty}$:

$$\mathcal{G}(\mathbf{c}^*, \mathbf{u}^*) \leqslant \liminf_{k\to\infty} \mathcal{G}(\mathbf{c}^k, \mathbf{u}^k) = m,$$

i.e., $(\mathbf{c}^*, \mathbf{u}^*)$ is a minimizer of the functional $\mathcal{G}$. □

Note that the $\mathbf{c} = (c_{11}, c_{10}, c_{01}, c_{00})$ values given in the above theorem are computed in the numerical scheme based on the dual minimization formulation of Chambolle [43] and extends [42] which is described in detail in Section 3.1.

References

[1] T.F. Chan, S. Esedoglu, M. Nikolova, Algorithms for finding global minimizers of image segmentation and denoising models, SIAM J. Appl. Math. 66 (2006) 1632–1648.
[2] T.F. Chan, L.A. Vese, Active contours without edges, IEEE Trans. Image Process. 10 (2001) 266–277.
[3] D. Mumford, J. Shah, Optimal approximations by piecewise smooth functions and associated variational problems, Commun. Pure Appl. Math. 42 (1989) 577–685.
[4] T.F. Chan, B.Y. Sandberg, L.A. Vese, Active contours without edges for vector-valued images, J. Visual Commun. Image Represent. 11 (2000) 130–141.
[5] L. Vese, T.F. Chan, A multiphase level set framework for image segmentation using the Mumford and Shah model, Int. J. Comput. Vis. 50 (2002) 271–293.
[6] M.S. Keegan, B. Sandberg, T.F. Chan, A multiphase logic framework for multichannel image segmentation, Inverse Problems Imag. 6 (2012) 95–110.
[7] D.S. Marcus, J. Harwell, T. Olsen, M. Hodge, M.F. Glasser, F. Prior, M. Jenkinson, T. Laumann, S.W. Curtiss, D.C.V. Essen, Informatics and data mining tools and strategies for the human connectome project, Frontiers Neuroinform. 5 (2011) 1–12.
[8] S. Osher, J.A. Sethian, Fronts propagating with curvature-dependent speed: algorithms based on Hamilton-Jacobi formulations, J. Comput. Phys. 79 (1988) 12–49.
[9] C.S. Drapaca, V. Cardenas, C. Studholme, Segmentation of tissue boundary evolution from brain MR image sequences using multi-phase level sets, Comput. Vis. Image Understand. 100 (2005) 312–329.
[10] S.K. Nath, K. Palaniappan, Fast graph partitioning active contours for image segmentation using histograms, EURASIP J. Image Video Process. (2009) 9.
[11] J. Koh, P.D. Scott, V. Chaudhary, G. Dhillon, An automatic segmentation method of the spinal canal from clinical MR images based on an attention model and an active contour model, in: ISBI, Chicago, IL, USA, 2011, pp. 1467–1471. http://dx.doi.org/10.1109/ISBI.2011.5872677.
[12] L. Gui, R. Lisowski, T. Faundez, P.S. Huppi, Automatic segmentation of newborn brain MRI using mathematical morphology, in: ISBI, Chicago, IL, USA, 2011, pp. 2026–2030. http://dx.doi.org/10.1109/ISBI.2011.5872810.
[13] M.N. Ahmed, S.M. Yamany, N. Mohamed, A.A. Farag, T. Moriarty, A modified fuzzy c-means algorithm for bias field estimation and segmentation of MRI data, IEEE Trans. Med. Imag. 21 (2002) 193–199.
[14] A.W.-C. Liew, H. Yan, An adaptive spatial fuzzy clustering algorithm for 3-D MR image segmentation, IEEE Trans. Med. Imag. 22 (2003) 1063–1075.
[15] K.-S. Chuang, H.-L. Tzeng, S. Chen, J. Wu, T.-J. Chen, Fuzzy c-means clustering with spatial information for image segmentation, Comput. Med. Imag. Graphics 30 (2006) 9–15.
[16] F. Bunyak, A. Hafiane, K. Palaniappan, Histopathology tissue segmentation by combining fuzzy clustering with multiphase vector level sets, in: H.R. Arabnia, Q.N. Tran (Eds.), Software Tools and Algorithms for Biological Systems, Advances in Experimental Medicine and Biology, vol. 41, Springer, 2011, pp. 413–424.
[17] Y. Zhuge, J.K. Udupa, Intensity standardization simplifies brain MR image segmentation, Comput. Vis. Image Understand. 113 (2009) 1095–1103.
[18] B. Fischl, D.H. Salat, E. Busa, M. Albert, M. Dieterich, C. Haselgrove, A. van der Kouwe, R. Killiany, D. Kennedy, S. Klaveness, et al., Whole brain segmentation: automated labeling of neuroanatomical structures in the human brain, Neuron 33 (2002) 341–355.
[19] W. Wells III, W.E.L. Grimson, R. Kikinis, F.A. Jolesz, Adaptive segmentation of MRI data, IEEE Trans. Med. Imag. 15 (1996) 429–442.
[20] J.L. Marroquin, B.C. Vemuri, S. Botello, E. Calderon, A. Fernandez-Bouzas, An accurate and efficient Bayesian method for automatic segmentation of brain MRI, IEEE Trans. Med. Imag. 21 (2002) 934–945.
[21] Y. Zhang, M. Brady, S. Smith, Segmentation of brain MR images through a hidden Markov random field model and the expectation-maximization algorithm, IEEE Trans. Med. Imag. 20 (2001) 45–57.
[22] L. Liao, T. Lin, B. Li, MRI brain image segmentation and bias field correction based on fast spatially constrained kernel clustering approach, Pattern Recogn. Lett. 29 (2008) 1580–1588.
[23] F.A. Cappabianco, A.X. Falcao, C.L. Yasuda, J.K. Udupa, Brain tissue MR-image segmentation via optimum-path forest clustering, Comput. Vis. Image Understand. 116 (2012) 1047–1059.
[24] M.S. Atkins, B.T. Mackiewich, Fully automatic segmentation of the brain in MRI, IEEE Trans. Med. Imag. 17 (1998) 98–107.
[25] U. Amato, M. Larobina, A. Antoniadis, B. Alfano, et al., Segmentation of magnetic resonance brain images through discriminant analysis, J. Neurosci. Methods 131 (2003) 65–74.
[26] S. Shen, W. Sandham, M. Granat, A. Sterr, MRI fuzzy segmentation of brain tissue using neighborhood attraction with neural-network optimization, IEEE Trans. Inform. Technol. Biomed. 9 (2005) 459–467.
[27] N.R. Pal, S.K. Pal, A review on image segmentation techniques, Pattern Recogn. 26 (1993) 1277–1294.
[28] D.L. Pham, C. Xu, J.L. Prince, Current methods in medical image segmentation, Ann. Rev. Biomed. Eng. 2 (2000) 315–337.
[29] Z. Ma, J.M.R.S. Tavares, R.N.M. Jorge, T. Mascarenhas, A review of algorithms for medical image segmentation and their applications to the female pelvic cavity, Comput. Methods Biomech. Biomed. Eng. 13 (2010) 235–246.
[30] M.A. Balafar, A. Ramli, M.I. Saripan, S. Mashohor, Review of brain MRI image segmentation methods, Artif. Intell. Rev. 33 (2010) 261–274.

[31] A. Hafiane, F. Bunyak, K. Palaniappan, Clustering initiated multiphase active contours and robust separation of nuclei groups for tissue segmentation, in: IEEE International Conference on Pattern Recognition, 2008, pp. 1–4. http://dx.doi.org/10.1109/ICPR.2008.4761744.
[32] G. Dogan, P. Morin, R.H. Nochetto, A variational shape optimization approach for image segmentation with a Mumford-Shah functional, SIAM J. Scient. Comput. 30 (2008) 3028–3049.
[33] F. Bunyak, K. Palaniappan, Efficient segmentation using feature-based graph partitioning active contours, in: 12th IEEE International Conference on Computer Vision, Kyoto, Japan, 2009, pp. 873–880. http://dx.doi.org/10.1109/ICCV.2009.5459320.
[34] E. Brown, T.F. Chan, X. Bresson, A convex relation method for a class of vector-valued minimization problems with applications to Mumford-Shah segmentation, Technical Report 43, UCLA CAM, 2010.
[35] E.S. Brown, T.F. Chan, X. Bresson, Completely convex formulation of the Chan-Vese image segmentation model, Int. J. Comput. Vis. 98 (2012) 103–121.
[36] J.C. Moreno, Contributions to Variational Image Segmentation, Ph.D. Thesis, University of Coimbra, Portugal, 2012.
[37] S.H. Kang, R. March, Existence and regularity of minimizers of a functional for unsupervised multiphase segmentation, Nonlinear Anal.: Theory, Methods Appl. 76 (2013) 181–201.
[38] C. Zach, D. Gallup, J.-M. Frahm, M. Niethammer, Fast global labeling for real-time stereo using multiple plane sweeps, in: Proceedings of Vision, Modeling, and Visualization, Konstanz, Germany, 2008, pp. 243–252.
[39] J. Lellman, J. Kappes, J. Yuang, F. Becker, C. Schnörr, Convex multi-class image labeling by simplex-constrained total variation, in: Scale Space and Variational Methods in Computer Vision, vol. 5567, Voss, Norway, 2009, pp. 150–162. http://dx.doi.org/10.1007/978-3-642-02256-2_13.
[40] E. Bae, J. Yuan, X.-C. Tai, Global minimization for continuous multiphase partitioning problems using a dual approach, Int. J. Comput. Vis. 92 (2011) 112–129.
[41] A. Chambolle, D. Cremers, T. Pock, A convex approach to minimal partitions, SIAM J. Imag. Sci. 5 (2012) 1113–1158.
[42] X. Bresson, S. Esedoglu, P. Vandergheynst, J. Thiran, S. Osher, Fast global minimization of the active contour/snake model, J. Math. Imag. Vis. 28 (2007) 151–167.
[43] A. Chambolle, An algorithm for total variation minimization and applications, J. Math. Imag. Vis. 20 (2004) 89–97.
[44] J.-F. Aujol, G. Gilboa, T. Chan, S. Osher, Structure-texture image decomposition – modeling, algorithms and parameter selection, Int. J. Comput. Vis. 67 (2006) 111–136.
[45] S. Merino-Caviedes, G. Vegas-Sanchez, M. Perez, S. Aja-Fernandez, M. Martin-Fernandez, Automatic segmentation of newborn brain MRI using mathematical morphology, in: ISBI, Rotterdam, 2010, pp. 908–911. http://dx.doi.org/10.1109/ISBI.2010.5490134.
[46] M. Ben Salah, A. Mitiche, I. Ben Ayed, Effective level set image segmentation with a kernel induced data term, IEEE Trans. Image Process. 19 (2010) 220–232.
[47] I.B. Ayed, A. Mitiche, A region merging prior for variational level set image segmentation, IEEE Trans. Image Process. 17 (2008) 2301–2311.
[48] A. Chambolle, T. Pock, A first-order primal-dual algorithm for convex problems with applications to imaging, J. Math. Imag. Vis. 40 (2011) 120–145.
[49] J.-F. Aujol, A. Chambolle, Dual norms and image decomposition models, Int. J. Comput. Vis. 63 (2005) 85–104.
[50] C. Li, C.-Y. Kao, J.C. Gore, Z. Ding, Minimization of region-scalable fitting energy for image segmentation, IEEE Trans. Image Process. 17 (2008) 1940–1949.
[51] N. Zhang, S. Ruan, S. Lebonvallet, Q. Liao, Y. Zhu, Kernel feature selection to fuse multi-spectral MRI images for brain tumor segmentation, Comput. Vis. Image Understand. 115 (2011) 256–269.
[52] I.N. Figueiredo, J.C. Moreno, V.B.S. Prasath, P.N. Figueiredo, A segmentation model and application to endoscopic images, in: A. Campilho, M. Kamel (Eds.), International Conference on Image Analysis and Recognition (ICIAR 2012), Aveiro, Portugal, LNCS, vol. 7325, Springer, 2012, pp. 164–171. http://dx.doi.org/10.1007/978-3-642-31298-4_20.
[53] I.N. Figueiredo, J.C. Moreno, V.B.S. Prasath, Texture image segmentation with smooth gradients and local information, in: Computational Modeling of Objects Presented in Images: Fundamentals, Methods and Applications (ComplMAGE 2012), Rome, Italy, 2012, pp. 164–171.
[54] V.B.S. Prasath, F. Bunyak, P.S. Dale, S.R. Frazier, K. Palaniappan, Segmentation of breast cancer tissue microarrays for computer-aided diagnosis in pathology, in: First IEEE Healthcare Technology Conference: Translational Engineering in Health & Medicine, Houston, TX, USA, 2012, pp. 40–43.
[55] V.B.S. Prasath, K. Palaniappan, G. Seetharaman, Multichannel texture image segmentation using weighted feature fitting based variational active contours, in: Eighth Indian Conference on Vision, Graphics and Image Processing (ICVGIP), Mumbai, India, 2012, pp. 78:1–78:6. http://dx.doi.org/10.1145/2425333.2425411.
[56] F. Giusti, Minimal Surfaces and Functions of Bounded Variation, Birkhauser, Basel, Switzerland, 1984.
[57] R.-S. Kwan, A. Evans, G. Pike, MRI simulation-based evaluation of image-processing and classification methods, IEEE Trans. Med. Imag. 18 (1999) 1085–1097.
[58] R. Unnikrishnan, C. Pantofaru, M. Hebert, Toward objective evaluation of image segmentation algorithms, IEEE Trans. Pattern Anal. Mach. Intell. 29 (2007) 929–944.
[59] L.R. Dice, Measures of the amount of ecologic association between species, Ecology 26 (1945) 297–302.
[60] T.F. Chan, S. Esedoglu, Aspects of total variation regularized L1 function approximation, SIAM J. Appl. Math. 65 (2005) 1817–1837.
[61] M. Jung, M. Kang, M. Kang, Variational image segmentation model involving non-smooth data-fidelity terms, J. Scient. Comput., 2014.
[62] H. Attouch, G. Buttazzo, G. Michaille, Variational analysis in Sobolev and BV spaces: applications to PDEs and optimization, Society for Industrial and Applied Mathematics, SIAM, Philadelphia, PA, USA, 2006.
[63] G. Aubert, P. Kornprobst, Mathematical Problems in Image Processing: Partial Differential Equation and Calculus of Variations, Springer-Verlag, New York, USA, 2006.